Author's Accepted Manuscript

Water flow prediction for Membranes using 3D simulations with detailed morphology

Meixia Shi, Galina Printsypar, Oleg Iliev, Victor M. Calo, Gary L. Amy, Suzana P. Nunes

Cite this article as: Meixia Shi, Galina Printsypar, Oleg Iliev, Victor M. Calo, Gary L. Amy, Suzana P. Nunes, Water flow prediction for Membranes using 3D simulations with detailed morphology, *Journal of Membrane Science*, http://dx.doi.org/10.1016/j.memsci.2015.03.036

Water Flow Prediction for Membranes Using 3D Simulations

with Detailed Morphology

Meixia Shi[a,b], Galina Printsypar[a], Oleg Iliev[a,c], Victor M. Calo[a,d,*], Gary L. Amy[b], Suzana P. Nunes[b,*]

[a] *Center for Numerical Porous Media, King Abdullah University of Science and Technology, Thuwal 23955-6900, Saudi Arabia*

[b] *Water Desalination and Reuse Center, King Abdullah University of Science and Technology, Thuwal 23955-6900, Saudi Arabia*

[c] *Flows and Materials Simulation Department, Fraunhofer Institute for Industrial Mathematics, Kaiserslautern 67663, Germany*

[d] *Applied Mathematics & Computational Science, and Earth Science & Engineering, King Abdullah University of Science and Technology, Thuwal 23955-6900, Saudi Arabia*

Corresponding author: Tel: +966 12 8082771, email: Suzana.Nunes@kaust.edu.sa

(S. P. Nunes); Tel: +966 12 8080315, email: Victor.Calo@kaust.edu.sa (V. M. Calo).

Highlights

- New predictive framework to model membranes' water permeance

- 3D membrane morphologies resolved at the pore scale

- Stokes and Stokes-Brinkman models applied to compute 3D velocity distributions

- Realistic 3D approach for water permeance evaluation

Abstract

The membrane morphology significantly influences membrane performance. For osmotically driven membrane processes, the morphology strongly affects the internal concentration polarization. Different membrane morphologies were generated by simulation and their influence on membrane performance was studied, using a 3D model. The simulation results were experimentally validated for two classical phase-inversion membrane morphologies: sponge- and finger-like structures. Membrane porosity and scanning electron microscopy image information were used as model input. The permeance results from the simulation fit well the experimentally measured permeances. Water permeances were predicted for different kinds of finger-like cavity membranes with different finger-like cavity lengths and various finger-like cavity sets, as well as for membranes with cylindrical cavities. The results provide realistic information on how to increase water permeance, and also illustrate that membrane's complete morphology is important for the accurate water permeance evaluation. Evaluations only based on porosity might be misleading, and the new 3D simulation approach gives a more realistic representation.

Keywords: morphology; simulation; porosity; polyacrylonitrile; water

Nomenclature

K Darcy permeability

ε membrane porosity

m_{wet} mass of the wet membrane

m_{dry} mass of the dry membrane

ρ_w density of water

ρ_p density of polyacrylonitrile

ΔP pressure difference across the membrane

S slope of the relationship between the mass and the time

J_w water permeance

A membrane area

ϕ finger void percentage

ϕ_s porosity of the bulk sponge-like media

p pressure

μ dynamic viscosity

μ_{eff} effective viscosity

u velocity

k_{micro} Darcy permeability of microporous walls for a finger-like cavity membrane

Q volumetric flow rate

L membrane thickness

K_1 Darcy permeability of the selective layer

K_2 Darcy permeability of the support layer

L_1 thickness of the selective layer

L_2 thickness of the support layer

PAN   polyacrylonitrile

DMF   N, N-dimethylformamide

NMP   N-methyl-2-pyrrolidone

FESEM   field emission scanning electron microscopy

1. Introduction

The membrane morphology determines permeance and solute rejection in pressure-driven technologies for water treatment, such as ultra- and nano-filtration.

3

For osmotically driven membrane processes such as forward osmosis and pressure retarded osmosis, the membrane structure is even more important due to internal concentration polarization [1-3]. For osmotically driven processes in order to achieve high water flux, membranes are manufactured with multilayers: a thin dense and selective layer frequently prepared by interfacial polymerization, a porous asymmetric support and in some cases an additional non-woven. The structure of the porous layer might largely affect the performance [4-6]. In many studies, an essential goal is to achieve a better understanding on how changes in morphology lead to improved fluxes, and/or to establish correlations between the characteristics of the porous media (porosity, anisotropy, tortuosity) and the permeance.

For many years, approximate analytical formulae (such as Kozeny-Carman model [7, 8].) have been used to correlate the membrane morphology and the fluxes through it. Such formulae, however, are based on simplifying assumptions on the shape of pores. For example, the Kozeny-Carman relation appropriately models the flow around spherical obstacles. Another popular model the Hagen-Poiseuille equation assumes uniform cylindrical pores [9].

Two-dimensional simulations of membrane have been previously conducted by other groups [10-12]. Wang et al. [10] studied membrane surface properties such as porosity and pore distribution, and found relations between the experimentally measured pore properties and flow properties (water flux and rejection). Sun et al. [11] measured the water flux and calculated the average pore size based on the Hagen-Poiseuille equation. Vicente et al. [13] studied both 2D and 3D ceramic microfiltration membranes, however, they used only one specific layer geometry.

4

Fluid simulation through membranes has been widely studied but mainly in macro scale and focusing on flow channels [14-16]. Most cases determine the membrane's Darcy permeability from empirical evidence [14, 17, 18]. The authors of those papers mainly highlight the mass transfer (water flux and solute rejection), while the membrane is usually simplified and modeled based on averaged porous media properties, without taking the detailed morphology into consideration and estimating the Darcy permeability from experiments. This approach, despite very useful, does not help to understand the link between the membrane morphology and the permeance. The Darcy permeability (K, [m^2]) is an intrinsic material property and solely depends on the membrane's properties (such as porosity, pore size distribution, anisotropy, and tortuosity) but is not affected by neither the viscosity of the permeating liquid nor by the size of membrane sample [19]. Furthermore, Darcy permeability is a scalar value for isotropic porous media, but it is a full tensor for anisotropic media [20]. For example, tubular membranes have different permeability values across and along the direction of the tubes in the membrane. The Darcy permeability differs from the permeance and permeability coefficient more commonly used by membrane researchers, as defined by Koros et al. [21]. Both the permeance and the permeability coefficient can be considered as process parameters and therefore they depend on the properties of the permeating fluid and membrane dimensions [19].

In our work, 3D membrane morphologies, resolved at the pore scale, were studied via experiments and simulations. We present a computational methodology to calculate the permeability of membranes depending on their 3D microstructure (morphology), as well as to validate the simulation results in comparison with measurements. This computational methodology has been used recently in other fields of porous media

research (e.g., hydrology [22, 23], oil recovery [24-26], and hygienic materials [27, 28]). We adapted the technology to the needs of membrane science and demonstrated its predictive power. The water flow through these membrane morphologies was investigated by solving Stokes and Stokes-Brinkman equations, which describe slow laminar flow of an incompressible fluid through a porous structure. The simulation and experimental results for sponge- and finger-like structures were compared. These morphologies are commonly described in the literature [29-31]. Furthermore, the introduced simulation methodology was applied to predict the performance of hybrid morphologies and other unexplored structures, before efforts are dedicated to manufacturing them experimentally. In addition to gaining insight into the performance of different membranes, the computational results illustrate the fact that water permeance predictions only based on porosity may be misleading, and in certain cases only a detailed computational study of the permeance may provide instructive results.

2. Experimental

2.1 Materials and chemicals

Polyacrylonitrile (PAN, Mw=324 000 g/mol) was used for membrane fabrication. N, N-dimethylformamide (DMF, anhydrous, ≥99.8%) and N-methyl-2-pyrrolidone (NMP, anhydrous, 99.5%) were purchased from Sigma-Aldrich. Milli-Q ultrapure water was used in the flow tests.

2.2 Membrane fabrication

Two different casting solutions and two different precipitation baths were used for membrane fabrication. Two kinds of membranes were generated using 12 wt % and 16 wt % polyacrylonitrile cast solutions and two different precipitation baths (water

and volumetric 1:1 water/NMP). Details are listed in Table 1. Besides PAN, other polymers can also be prepared and form different membrane morphologies via similar methods [32].

Table 1. Membrane fabrication conditions.

Membrane morphology	Cast solution compositions	Precipitation bath compositions
Sponge-like	16 wt% PAN in DMF	50 v% water + 50 v% NMP
Finger-like	12 wt% PAN in DMF	water

All casting solutions were stirred overnight at 60°C. They were kept without heating and stirring for up to 6 hours to remove air bubbles. The membrane was fabricated by phase inversion. The casting solution was cast on a glass plate with a gap of 200 µm. Immediately after casting, the glass plate was immersed into the corresponding precipitation bath. After the membrane had been detached from the glass plate, it was completely rinsed and stored in MQ water.

2.3 Morphology study

Surface and cross section morphologies of the fabricated membranes were imaged by field emission scanning electron microscopy (FESEM) on Nova Nano FEI equipment. Wet samples were kept in a freezer for 5 hours. Afterwards, they were transferred to a vacuum desiccator, where liquid nitrogen was poured into the bottom. A vacuum pump was used immediately to remove icy water directly from the membrane. Lastly, the membrane surface and cross section samples were prepared using these treated membranes. All samples were coated with platinum using a sputter.

2.4 Porosity measurement

To obtain the porosity of the membrane, the mass of wet and dry membranes was measured. The excess of water on the wet membrane surface was carefully removed, and the membrane was weighed. Afterwards, the membrane was dried under vacuum at 60°C for three days. Then, it was weighed again. The measurements were performed for three different pieces of the same kind of membrane to obtain reliable average membrane porosity. The porosity ε measured in [%] was calculated as follows:

$$\varepsilon = \frac{(m_{wet} - m_{dry})/\rho_w}{(m_{wet} - m_{dry})/\rho_w + m_{dry}/\rho_p} \times 100\% \tag{1}$$

where m_{wet} and m_{dry} is the mass of the wet and dry membranes, respectively; ρ_w and ρ_p is the density of water and PAN, respectively (ρ_w = 1 g/cm^3, ρ_p = 1.184 g/cm^3).

2.5 Water permeance test

The water permeance test for the membranes was performed using lab-scale nano-/ultra-filtration dead-end setup. Pure water flux was applied under the pressure of 2 bar (ΔP, [bar]). The permeate weight was automatically collected by the balance to the connected computer every minute. The slope (S, [L h^{-1}]) was measured as the relationship between the mass and the time. Then, the water permeance J_w in [L m^{-2} h^{-1} bar^{-1}] was calculated as follows:

$$J_w = \frac{S}{A \times \Delta P}$$
(2)

where the membrane area is denoted by A measured in [m^2]. In the experimental setup, A was equal to 4.1×10^{-4} m^2.

3. Modeling

3.1 Digital membrane generation

We model an integral porous asymmetric membrane, which has two main layers: a thin selective porous layer and a thicker more porous support layer. In membrane processes, the selective layer plays a dominant role in rejecting the solute, and the support layer mainly provides mechanical stability to the selective layer. Therefore, in the simulations we treat the two layers separately.

3.1.1 Membrane surface analysis and selective layer generation

Pore distribution analysis for the membrane surface was done initially by adjusting the different tolerances of the gray values so that the chosen marked pores would reasonably represent the pores in the SEM images. Pore noise data whose area was less than five nm^2 $(=5\times10^{-18}$ $m^2)$ was eliminated. Finally, the surface porosity was estimated by calculating the pore area over the total membrane surface area.

Regarding the selective layer, in order to better reflect the real structure of polymeric membranes, some assumptions were made: (a) The selective layer is constituted itself by two layers with different porosities, the top one having smaller pores. (b) Regarding the top layer, we consider a thickness with the same order of magnitude of the average surface pore size; it is symmetric (all pores in this layer were considered cylinders); the surface porosity was treated as volumetric. (c) Regarding the second selective intermediate layer, the geometry was considered porous sponge-like and the pore size was the harmonic mean between the top selective layer and the non-selective much thicker support layer. The thickness of the selective intermediate layer was 500 nm. Given the low porosity of the selective layer and the regularity of the pore sizes and distribution, the modeling assumptions described above are

reasonable. To verify these assumptions we also tested the impact of switching between circular and ellipsoidal pores and the difference in the simulation results is well within the uncertainty of the experimental measurements.

3.1.2 Support layer generation

FESEM images were used to determine the membrane's thickness and the size, shape, and distribution of its pores. The membrane porosity was estimated from the experiment described in Section 2.4. The porosity is the ratio of the volume of all pores (including finger-like cavities and sponge pores) to the membrane volume, while finger void percentage is the ratio of the volume of the finger-like cavities to the membrane volume. The finger void percentage for the finger-like cavity membrane can be calculated based on its membrane porosity ε via Eq. (3), where ϕ is the finger void percentage, and ϕ_s is the porosity of the bulk sponge-like media. Both SEM image information and porosity were fed in the software GeoDict (Math2Market GmbH, Germany) to generate 3D digital membranes with resolved morphology. In water permeance prediction described in Section 4.5, the finger void percentage can be directly obtained based on the generated morphology in GeoDict, while the membrane porosity can be calculated by the transformation of Eq. (3). Besides the digital membrane creation, GeoDict was also used for the flow simulation in Section 3.2.

$$\varnothing = \frac{\varepsilon - \varnothing_s}{1 - \varnothing_s} \qquad \text{or} \qquad \text{its} \qquad \text{transformation:} \qquad \varepsilon = \varnothing + (1 - \varnothing) \times \varnothing_s$$

(3)

3.2 Governing equations of the flow at the pore scale

To describe the flow at the pore scale in the case of the selective layer, as well as in the cases of sponge, nanofibers, and woven support layers, the Stokes system of equations (Eq. (4)) was used:

$$-\mu\nabla^2 u + \nabla p = 0; \qquad \nabla^2 u = 0 \tag{4}$$

For the finger-like cavity membrane, in order to account for the microporous walls, the Stokes-Brinkman system of equations (Eq. (5)) was used [33]. Stokes-Brinkman equations were also applied to calculate the Darcy permeability for the whole layered membrane.

$$-\mu_{eff}\nabla^2 u + \mu k_{micro}^{-1} u + \nabla p = 0; \qquad \nabla^2 u = 0 \tag{5}$$

In equations (4) and (5), p is the pressure; μ is the dynamic viscosity; μ_{eff} is the effective viscosity (defined as the dynamic viscosity divided by the porosity); u is the velocity vector; and k_{micro} is the Darcy permeability of the microporous walls for a finger-like cavity membrane. The Stokes and Stokes-Brinkman models were supplemented with a set of boundary conditions. Periodic boundary conditions for the pressure and the velocity were used in all directions. In the flow direction, the periodic boundary condition for the pressure included a constant pressure drop, which represented the overall pressure gradient along the flow direction. A no-slip velocity was applied to the velocity field at the solid-fluid interface in the case of Stokes equations. This assumption stated that the flow velocity at the pore or cavity walls was equal to zero. Equations (4) and (5) were further used to find the distributions of the flow velocity and the pressure.

To compute the Darcy permeability K of the full layer system, namely selective and support layers, Darcy's law was applied using the following:

$$Q = \frac{-KA}{\mu}\frac{\Diamond P}{L}$$

(6)

where Q is the volumetric flow rate; A is the area; L is the membrane thickness; and $\Diamond P$ is the pressure difference across the membrane. The vertical direction (perpendicular to the membrane surface) was considered to be the flow direction. The fluid flow and the permeability value were calculated only in this direction. The simulations were run at a pressure drop of 0.02 Pa. The temperature for the model and experiment was set at 20°C.

4. Results and Discussion

4.1 Two membrane morphologies

By using the conditions listed in Table 1, two different membrane morphologies were fabricated: sponge- and finger-like structures. Fig. 1 shows two different membrane morphologies (cross sections), and highlights the pores in the bulk. The finger-like structure has a higher porosity than the sponge-like structure. This was quantified by measuring the weight of water saturating the pores. Figures 1 (c) and 1 (d) show that the pore structure in the bulk of the sponge-like membrane and that of the regions between the large finger-like cavities are similar. Therefore, the Darcy permeability of the support layer in the sponge-like structure was also applied to regions between the finger-like cavities.

Fig. 1. FESEM cross section images of the two main membrane morphologies investigated herein: (a) sponge-like membrane; (b) finger-like cavity membrane; (c) higher magnification of Fig. 1(a), showing details of the sponge-like membrane cross section; (d) higher magnification of Fig. 1(b), showing regions between finger-like cavities.

4.2 Membrane porosity

From the experiments described in Section 2.4, the membrane porosity was calculated and is reported in Table 2. The finger-like cavity membrane has higher overall porosity than that of the sponge-like membrane.

Table 2. Membrane porosity.

Membrane morphology	Porosity (%)
Sponge-like	72.4 ± 0.6
Finger-like	84.6 ± 0.2

The surface porosity was estimated from the SEM images shown in Fig. 2. The imaged pores were highlighted in red and the porosity was calculated from the ratio of the total pore area divided by the membrane surface area. The sponge-like membrane top surface porosity is 3.3%, while the finger-like cavity membrane top surface porosity is 5.1%.

Fig. 2. Membrane surface analysis: (a) original sponge-like membrane surface; (b) original finger-like cavity membrane surface; (c) sponge-like membrane surface with marked pores; (d) finger-like cavity membrane surface with marked pores.

4.3 Digital membranes and velocity distribution

The membranes experimentally prepared here were asymmetric, as most polymeric porous ultrafiltration membranes. As explained in Section 3.1, for the simulation the membranes were divided in two layers: a selective layer and a support layer. Fig. 3

13

shows the top surface pore distribution and the cross section pore morphology digitally generated for the two kinds of membranes we analyze herein.

Based on the generated digital membrane, flow simulations were carried out. Fig. 4 shows the detailed velocity magnitude distribution in three dimensions within the support layer of the sponge-like membrane. Fig. 5 shows the analogous information of velocity magnitude distribution for the finger-like cavity membrane. The support layer is asymmetric and the images are sliced to show the velocity changes in different planes or sublayers parallel and orthogonal to the membrane surface.

Fig. 3. Digitally generated membranes corresponding to those experimentally manufactured and shown in Figs. 1 and 2: (a) sponge-like membrane surface; (b) finger-like cavity membrane surface; (c) cross sections for the sponge-like and finger-like cavity membranes.

Fig. 4. Three-dimensional velocity magnitude distributions (colored by velocity magnitude) for the sponge-like membrane (the polymer matrix is depicted light gray in the image). Left column shows from bottom to top (sublayers parallel to the membrane surface); right column shows from back to front (sublayers orthogonal to the membrane surface); bottom figure shows the entire simulated membrane domain.

Fig. 5. Three-dimensional velocity magnitude distributions for finger-like cavity membrane. Left column shows from bottom to top (sublayers parallel to the

membrane surface); right column shows from back to front (sublayers orthogonal to the membrane surface); bottom figure shows the entire simulated membrane domain.

Besides sponge- and finger-like structures, other membrane morphologies were generated in order to demonstrate the generality of the model. Fig. 6 shows structures corresponding to electrospun nanofiber membranes and woven supports, where the bright colorful images are the digitally generated membranes while the gray ones are real membrane images at the lower right corner in the first row. Nanofibers as depicted in Fig. 6 have been previously prepared in our group by electrospinning as reported by Maab et al. [34]. The woven structure image is adapted from [35]. Meanwhile, 3D velocity magnitude distributions are also shown in Fig. 6 at different depths in the membrane.

Fig. 6. Electrospun nanofibers (left column) and woven support (right column) for membranes. The first row shows the digital membrane; on the lower right corner of each column, an image of the manufactured membranes is added as an inset. The remaining rows show the velocity magnitude at different membrane depths.

4.4 Water permeance and Darcy permeability

The computed Darcy permeabilities for the selective layer and support layer of the sponge-like and finger-like cavity membranes are listed in Table 3. From the table, the Darcy permeability for the entire membrane was close to that of the support layer for both membranes. This is reasonable because the selective layer is much thinner

than the support layer. In the layered membrane system when only flow perpendicular to the membrane is considered, Eq. (7) describes the relationship between the total membrane's Darcy permeability, K, (considered here also as porous layer) and the selective layer's Darcy permeability, K_1, and the support layer's Darcy permeability, K_2; L_1 and L_2 are the thickness of the selective layer and of the support layer, respectively.

$$\frac{L_1 + L_2}{K} = \frac{L_1}{K_1} + \frac{L_2}{K_2}$$

(7)

In Eq. (7), the Darcy permeability of the entire membrane (the left side of the equation) is determined by the characteristics of the two component layers (the right side of the equation: the first term relates to the selective layer, and the second term relates to the support layer). Considering the real data, both for the sponge-like and finger-like cavity membranes, $L_1 \ll L_2$ (more than 2 orders of magnitude smaller), $K_1 < K_2$ (less than an order of magnitude smaller), hence $L_1/K_1 < L_2/K_2$ (more than an order of magnitude smaller), and the right side of the equation is mainly determined by the support layer. Thus, the total membrane's Darcy permeability is close to the support layer's value.

According to the Stokes and the Stokes-Brinkman models, the water permeance was estimated as 76 L m^{-2} h^{-1} bar^{-1} and 314 L m^{-2} h^{-1} bar^{-1} for the sponge-like and finger-like cavity membranes respectively. The water permeance measurement in a dead-end nano-/ultra-filtration setup was also summarized in Table 4. The simulated flux fits well with the experimental data.

Table 3. Darcy permeability and thickness of membranes.

Membrane		Thickness (μm)	Darcy permeability ($\times 10^{-17}$ m^2)
Sponge-like	Selective layer	0.512	0.315
	Support layer	62.0	1.36
	Total	62.5	1.32
Finger-like	Selective layer	0.513	0.846
	Support layer	85.0	7.82
	Total	85.5	7.45

Table 4. Experimental and simulated water permeance (J_w).

Membrane	Experimental J_w (L m^{-2} h^{-1} bar^{-1})	Simulated J_w (L m^{-2} h^{-1} bar^{-1})
Sponge-like	76 ± 1	76
Finger-like	322 ± 14	314

4.5 Water permeance prediction for alternative morphologies

To understand the impact of the morphology of the cavities on the water permeance, three different sets of simulations have been conducted. In all cases, the background structure corresponds to the sponge-like microporous structure, shown in Fig. 1(a), with a Darcy permeability of 1.36×10^{-17} m^2. The thickness of all membranes was fixed at 85 μm. Only the support layer of the membrane is studied in this section. In these sets of simulations we first analyzed the impact of the finger-like cavity length on

17

permeance. Second, we analyzed the impact of superposing several sets of cavities of different lengths. Lastly, we studied the impact of the cavity diameter on permeance. By repeating the simulation with different random seeds, when generating the digital membrane morphologies, water permeance values could be reproduced within 2 % difference.

4.5.1 Different finger-like cavity lengths

Four different lengths of finger-like cavities were studied: 0 μm (no finger), 24 μm (1/3 finger), 48 μm (2/3 finger), and 72 μm (full finger) as shown in Fig. 7. These are average values for the big finger-like cavities. Among them, the full finger-like cavity case was experimentally observed in the membrane we produced and showed in Fig. 1(b); similar membrane morphologies for other cases can be found in the literature [29, 36, 37]. Table 5 shows the membrane characteristics including Darcy permeability, water permeance, finger void percentage, and membrane porosity. As expected, Table 5 shows that finger void percentage and membrane porosity increase, when the finger-like cavity grows longer. As a result, the Darcy permeability increases, and the water permeance also increases. In order to study the impact of the cavity length on the water permeance, we maintain the same porosity and change the number of cavities. The simplified cavities (only the group of big cavities with the cylinder shape) are applied with fixed diameter but different lengths. Table 6 shows the water permeance for membranes with similar porosity, but different morphologies. The result presents a similar trend: a higher water permeance is obtained for longer fingers.

From this test, we can see that the membrane porosity usually grows when the finger-like cavity is enlarged. It is possible to keep the same membrane porosity, while changing the frequency and length of the finger-like cavities. The water

permeance increases if the length of the finger-like cavity increases at constant porosity.

Fig. 7. Digital finger-like cavity membranes with different finger lengths: (a) 0 µm (no finger-like cavity); (b) 24 µm finger-like cavities; (c) 48 µm finger-like cavities; (d) 72 µm finger-like cavities.

Table 5. Membrane characteristics based on different finger-like cavity lengths.

Finger-like cavity length	Darcy permeability ($\times 10^{-17}$ m^2)	Water permeance (L m^{-2} h^{-1} bar^{-1})	Finger void percentage (%)	Membrane porosity (%)
0 µm	1.36	58	0.0	72.0
24 µm	2.06	87	16.0	76.5
48 µm	4.65	197	31.4	80.8
72 µm	7.82	331	41.9	83.7

Table 6. Membrane characteristics for different cavity lengths but same porosity.

Cavity length	Darcy permeability ($\times 10^{-17}$ m^2)	Water permeance (L m^{-2} h^{-1} bar^{-1})	Finger void percentage (%)	Membrane porosity (%)
24 µm	1.85	78	12.8	75.9
48 µm	2.65	112	12.9	76.0
72 µm	4.69	199	12.9	76.0

4.5.2 Different finger-like cavity sets

Besides changing the finger-like cavity length, we considered membranes formed by sets of finger-like cavities of different lengths. The number of finger-like cavity sets was varied. One finger-like cavity set means that all cavities in the membrane have similar size and length. Different combinations of finger sets were considered, as shown in Fig. 8.

Fig. 8. Membranes built by combining different sets of finger-like cavities, each set has a different finger-like cavity length: (a) one finger-like cavity set; (b) two finger-like cavity sets; (c) three finger-like cavity sets; (d) four finger-like cavity sets.

The set with the longest finger-like cavities was included in all cases. To generate a more complex membrane structure, several extra smaller finger-like cavities were added. Among these cases, the membrane with two finger-like cavity sets was experimentally observed in the membrane we produced and showed in Fig. 1(b), similar membrane morphologies for other cases can be found in the literature [29, 38].

Table 7 shows the simulation results and the corresponding membrane characteristics. Both the finger void percentage and membrane porosity increase, as the number of added finger-like cavity sets increases. Darcy permeability increases gradually when the porosity rises, and so does the water permeance as shown in Fig. 9. The figure depicts the relationship between water permeance and membrane porosity, based on simulation data for two different factors: finger-like cavity length and number of finger-like cavity sets. Water permeance usually grows when the finger cavity becomes longer or more cavity sets are added.

Table 7. Membrane characteristics based on different numbers of finger-like cavity sets.

Number of sets	Darcy permeability ($\times 10^{-17}$ m^2)	Water permeance (L m^{-2} h^{-1} bar^{-1})	Finger void percentage (%)	Membrane porosity (%)
1	5.69	241	35.0	81.8
2	7.82	331	41.9	83.7
3	8.45	358	44.9	84.6

Fig. 9. Relationship between water permeance and membrane porosity.

4.5.3 Membranes with cylindrical cavities

Membranes with cylindrical cavities can be considered as idealized fingers holding the smallest tortuosity and lowest flow resistivity. Fig. 1(b) shows a real finger-like cavity membrane, with mainly two different finger sizes: larger ones with a diameter of approximately 17 µm and smaller ones with a diameter of approximately 10 µm. Membranes with two "cylinder" sizes as cavities were simulated. For each type, three different cases were investigated as shown in Fig. 10. Case one is a go-through cylindrical membrane, with all cylinders going from one side to the other through the entire membrane. Case two embeds a top sponge layer with 7µm thickness. Case three embeds a top and a bottom sponge layers, with 7 µm on the top and 6 µm thick on the bottom. 7 and 6 µm are average thicknesses for the top and bottom sponge layers, respectively, in the finger-like cavity membranes experimentally manufactured in this work. The same membrane porosity is maintained for all cases. The simulation results are displayed in Table 8. There is a huge difference in performance between the go-through cylindrical membrane and the other two cases.   As before, the most important aspect is the morphology, rather than the porosity to determine the permeance of the membrane.

Fig. 10. Membranes with cylindrical cavities: (a) go-through cylinders; (b) cylinders with top sponge layer; (c) cylinders with top and bottom sponge layers.

Table 8. Membrane characteristics for membranes with cylindrical cavities.

Membrane		Darcy permeability ($\times 10^{-17}$ m^2)	Water permeance (L m^{-2} h^{-1} bar^{-1})	Finger void percentage (%)	Membrane porosity (%)
17 µm cylinders	Go-through cylinders	278000	11800000	29.9	80.7
	Cylinders with top sponge layer	12.8	542	29.9	80.7
	Cylinders with top and bottom sponge layer	7.21	305	29.9	80.7
10 µm cylinders	Go-through cylinders	113000	4790000	29.9	80.7
	Cylinders with top sponge layer	15.0	635	29.9	80.7
	Cylinders with top and bottom sponge layer	7.85	332	29.9	80.7

Let us explain the results presented in Table 8. The simulation results for cylinders with top and bottom sponge layers demonstrate that membranes with the same porosity may have different Darcy permeabilities. That is, simple permeability formulae only based on porosity may not appropriately predict water permeance

values for membranes with different morphologies. Furthermore, the results initially may look counter-intuitive: the membrane with the big cylindrical channels has lower Darcy permeability, than the membrane with smaller channels. However when the top layer of the membrane has a sponge structure and the cylinders do not go through, the Darcy permeability is smaller for the bigger cylinders.

To understand this behavior we set up two simple test problems. We analyze structures of thickness 92 μm that have cylindrical channels with round corners and sponge walls embedded with 7 μm sponge layers on the top and on the bottom. The sponge has a Darcy permeability of 1.36×10^{-17} m^2. The first structure has one big cylindrical channel; while the second one has 4 smaller cylindrical channels (see Figs. 11 and 12, respectively). Both structures have approximately the same porosity. The velocity distributions for both tests are shown in Figs. 13 and 14. In Table 9 we present the Darcy permeability computed for both structures, which shows the same tendency of bigger permeability values for the smaller cylindrical channels we observed above. The explanation of these results in the case of closed channels can be found in the fact that the top and bottom sponge layers, closing the channels, are very thin. In this case, the water enters the channels not only from the top circular surfaces, which are just above each channel, but also from the surrounding ring. Because the smaller rings forming the cylindrical channels have a longer perimeter compared to the larger ring (for fixed porosity), the extra flow determines the difference in the permeability results (for illustration see Figs. 13 and 14).

Table 9. Membrane characteristics for different cylindrical cavities.

Membrane	Darcy permeability ($\times 10^{-17}$ m^2)	Water permeance (L m^{-2} h^{-1} bar^{-1})	Finger void percentage (%)	Membrane porosity (%)
1 cylinder	4.36	185	29.06	80.4
4 cylinders	4.70	199	28.45	80.3

Fig. 11. Test structure with 1 cylindrical channel with round corners.

Fig. 12. Test structure with 4 cylindrical channels with round corners.

Fig. 13. Velocity magnitude distribution for the structure with 1 cylindrical channel.

Fig. 14. Velocity magnitude distribution for the structure with 4 cylindrical channels.

5. Conclusions

Digital membranes were created based on typical morphologies for asymmetric membranes used in ultra-/nanofiltration, such as sponge- and finger-like structures. The simulated water permeance for each case was similar to the value obtained experimentally for analogous membranes. According to the simulation results, the water permeance for the sponge-like membrane investigated herein was much lower than that of finger-like cavity membranes. The layered membrane analysis shows that the total membrane's Darcy permeability is mainly determined by the support layer for this kind of phase-inversion membranes, since the thickness of this layer is much larger. The water permeance was then predicted for other structures, with different

finger-like cavity lengths and various finger-like cavity sets, as well as for cylindrical membranes.

Membrane porosity is a main factor to judge the membrane performance, such as the water permeance. The porosity can rise by enlarging the finger-like cavity or adding cavity sets. Water permeance grows as the porosity increases in this way.

In addition to the membrane porosity, the membrane morphology is also important. Our simulations indicate that the membrane's performance can vary for a fixed porosity if the membrane morphology changes.

Our simulations indicate that for fixed morphologies, formulae to determine the permeance can use porosity as a control factor. Nevertheless, these formulae should account for morphological changes if different kinds of membranes are going to be compared. As we have shown in several cases, membranes with comparable porosities can have widely different performances, depending on their morphologies.

References

[1] T.Y. Cath, A.E. Childress, M. Elimelech, Forward osmosis: principles, applications, and recent developments, Journal of Membrane Science, 281 (2006) 70-87.

[2] S. Zhao, L. Zou, C.Y. Tang, D. Mulcahy, Recent developments in forward osmosis: opportunities and challenges, Journal of Membrane Science, 396 (2012) 1-21.

[3] T.-S. Chung, S. Zhang, K.Y. Wang, J. Su, M.M. Ling, Forward osmosis processes: yesterday, today and tomorrow, Desalination, 287 (2012) 78-81.

[4] S. Zhang, K.Y. Wang, T.-S. Chung, H. Chen, Y.C. Jean, G. Amy, Well-constructed cellulose acetate membranes for forward osmosis: minimized internal concentration

polarization with an ultra-thin selective layer, Journal of Membrane Science, 360 (2010) 522-535.

[5] X. Song, Z. Liu, D.D. Sun, Nano gives the answer: breaking the bottleneck of internal concentration polarization with a nanofiber composite forward osmosis membrane for a high water production rate, Advanced Materials, 23 (2011) 3256-3260.

[6] K.Y. Wang, R.C. Ong, T.-S. Chung, Double-skinned forward osmosis membranes for reducing internal concentration polarization within the porous sublayer, Industrial & Engineering Chemistry Research, 49 (2010) 4824-4831.

[7] B. Fogelson, A. Mogilner, Computational estimates of membrane flow and tension gradient in motile cells, PloS one, 9 (2014) e84524.

[8] K. Knehr, E. Agar, C. Dennison, A. Kalidindi, E. Kumbur, A transient vanadium flow battery model incorporating vanadium crossover and water transport through the membrane, Journal of The Electrochemical Society, 159 (2012) a1446-a1459.

[9] M. Mulder, Basic principles of membrane technology (Second edition), Kluwer Academic Pub, 1996.

[10] L. Wang, X. Wang, Study of membrane morphology by microscopic image analysis and membrane structure parameter model, Journal of Membrane Science, 283 (2006) 109-115.

[11] W. Sun, T. Chen, C. Chen, J. Li, A study on membrane morphology by digital image processing, Journal of Membrane Science, 305 (2007) 93-102.

[12] S. Roy, R. Raju, H.F. Chuang, B.A. Cruden, M. Meyyappan, Modeling gas flow through microchannels and nanopores, Journal of Applied Physics, 93 (2003) 4870-4879.

[13] J. Vicente, Y. Wyart, P. Moulin, Characterization (two-dimensional–three-dimensional) of ceramic microfiltration membrane by synchrotron radiation: new and abraded membranes, Journal of Porous Media, 16 (2013) 537-545.

[14] M.F. Gruber, C.J. Johnson, C.Y. Tang, M.H. Jensen, L. Yde, C. Hélix-Nielsen, Computational fluid dynamics simulations of flow and concentration polarization in forward osmosis membrane systems, Journal of Membrane Science, 379 (2011) 488-495.

[15] G.A. Fimbres-Weihs, D.E. Wiley, Review of 3D CFD modeling of flow and mass transfer in narrow spacer-filled channels in membrane modules, Chemical Engineering and Processing: Process Intensification, 49 (2010) 759-781.

[16] H. Lotfiyan, F. Zokaee Ashtiani, A. Fouladitajar, S.B. Armand, Computational fluid dynamics modeling and experimental studies of oil-in-water emulsion microfiltration in a flat sheet membrane using Eulerian approach, Journal of Membrane Science, 472 (2014) 1-9.

[17] R.P. Castro, Y. Cohen, H.G. Monbouquette, The permeability behavior of polyvinylpyrrolidone-modified porous silica membranes, Journal of Membrane Science, 84 (1993) 151-160.

[18] K.J. Martin, D. Bolster, N. Derlon, E. Morgenroth, R. Nerenberg, Effect of fouling layer spatial distribution on permeate flux: a theoretical and experimental study, Journal of Membrane Science, 471 (2014) 130-137.

[19] P. Maarten Biesheuvel, H. Verweij, Design of ceramic membrane supports: permeability, tensile strength and stress, Journal of Membrane Science, 156 (1999) 141-152.

[20] J. Bear, Y. Bachmat, Introduction to modeling of transport phenomena in porous media, Springer, 1990.

[21] W. Koros, Y. Ma, T. Shimidzu, Terminology for membranes and membrane processes (IUPAC Recommendations 1996), Journal of Membrane Science, 120 (1996) 149-159.

[22] C. Butscher, P. Huggenberger, Implications for karst hydrology from 3D geological modeling using the aquifer base gradient approach, Journal of Hydrology, 342 (2007) 184-198.

[23] F. Khan, F. Enzmann, M. Kersten, A. Wiegmann, K. Steiner, 3D simulation of the permeability tensor in a soil aggregate on basis of nanotomographic imaging and LBE solver, Journal of Soils and Sediments, 12 (2012) 86-96.

[24] A. Georgiadis, S. Berg, A. Makurat, G. Maitland, H. Ott, Pore-scale micro-computed-tomography imaging: nonwetting-phase cluster-size distribution during drainage and imbibition, Physical Review E, 88 (2013) 033002.

[25] I. Bogdanov, J. Kpahou, I. Bondino, Image based pore-scale models of flow through porous media-oil recovery applications, ECMOR XIV-14th European Conference on the Mathematics of Oil Recovery, Catania, 2014.

[26] I. Bogdanov, J. Kpahou, F. Guerton, Pore-scale single and two-phase transport in real porous medium, ECMOR XIII-13th European Conference on the Mathematics of Oil Recovery, Biarritz, 2012.

[27] G. Zhang, H.C. Yang, W.D. Wei, Simulation of toothpaste flavor transportation in oral and nasal cavity during respiration, Applied Mechanics and Materials, 300 (2013) 195-198.

[28] E. Vennat, J.-P. Attal, D. Aubry, M. Degrange, Three-dimensional pore-scale modelling of dentinal infiltration, Computer Methods in Biomechanics and Biomedical Engineering, 17 (2014) 632-642.

[29] A. Tiraferri, N.Y. Yip, W.A. Phillip, J.D. Schiffman, M. Elimelech, Relating performance of thin-film composite forward osmosis membranes to support layer formation and structure, Journal of Membrane Science, 367 (2011) 340-352.

[30] S.H. Yoo, J.H. Kim, J.Y. Jho, J. Won, Y.S. Kang, Influence of the addition of PVP on the morphology of asymmetric polyimide phase inversion membranes: effect of PVP molecular weight, Journal of Membrane Science, 236 (2004) 203-207.

[31] J. Ren, Z. Li, Development of asymmetric BTDA-TDI/MDI (P84) copolyimide flat sheet and hollow fiber membranes for ultrafiltration: morphology transition and membrane performance, Desalination, 285 (2012) 336-344.

[32] Y. Xie, R. Tayouo, S.P. Nunes, Low fouling polysulfone ultrafiltration membrane via click chemistry, Journal of Applied Polymer Science, (2015) 41549.

[33] V. Laptev, Numerical solution of coupled flow in plain and porous media, PhD dissertation, University of Kaiserslautern, 2003.

[34] H. Maab, L. Francis, A. Al-saadi, C. Aubry, N. Ghaffour, G. Amy, S.P. Nunes, Synthesis and fabrication of nanostructured hydrophobic polyazole membranes for low-energy water recovery, Journal of Membrane Science, 423–424 (2012) 11-19.

[35] P. Vandeurzen, J. Ivens, I. Verpoest, A three-dimensional micromechanical analysis of woven-fabric composites: I. Geometric analysis, Composites Science and Technology, 56 (1996) 1303-1315.

[36] J.-F. Blanco, J. Sublet, Q.T. Nguyen, P. Schaetzel, Formation and morphology studies of different polysulfones-based membranes made by wet phase inversion process, Journal of Membrane Science, 283 (2006) 27-37.

[37] S. Madaeni, A. Rahimpour, Effect of type of solvent and non-solvents on morphology and performance of polysulfone and polyethersulfone ultrafiltration membranes for milk concentration, Polymers for Advanced Technologies, 16 (2005) 717-724.

[38] C.Y. Lai, A. Groth, S. Gray, M. Duke, Preparation and characterization of poly (vinylidene fluoride)/nanoclay nanocomposite flat sheet membranes for abrasion resistance, Water Research, 57 (2014) 56-66.

32

Highlights

- New predictive framework to model membranes' water permeance

- 3D membrane morphologies resolved at the pore scale

- Stokes and Stokes-Brinkman models applied to compute 3D velocity distributions

- More realistic 3D approach for water permeance evaluation
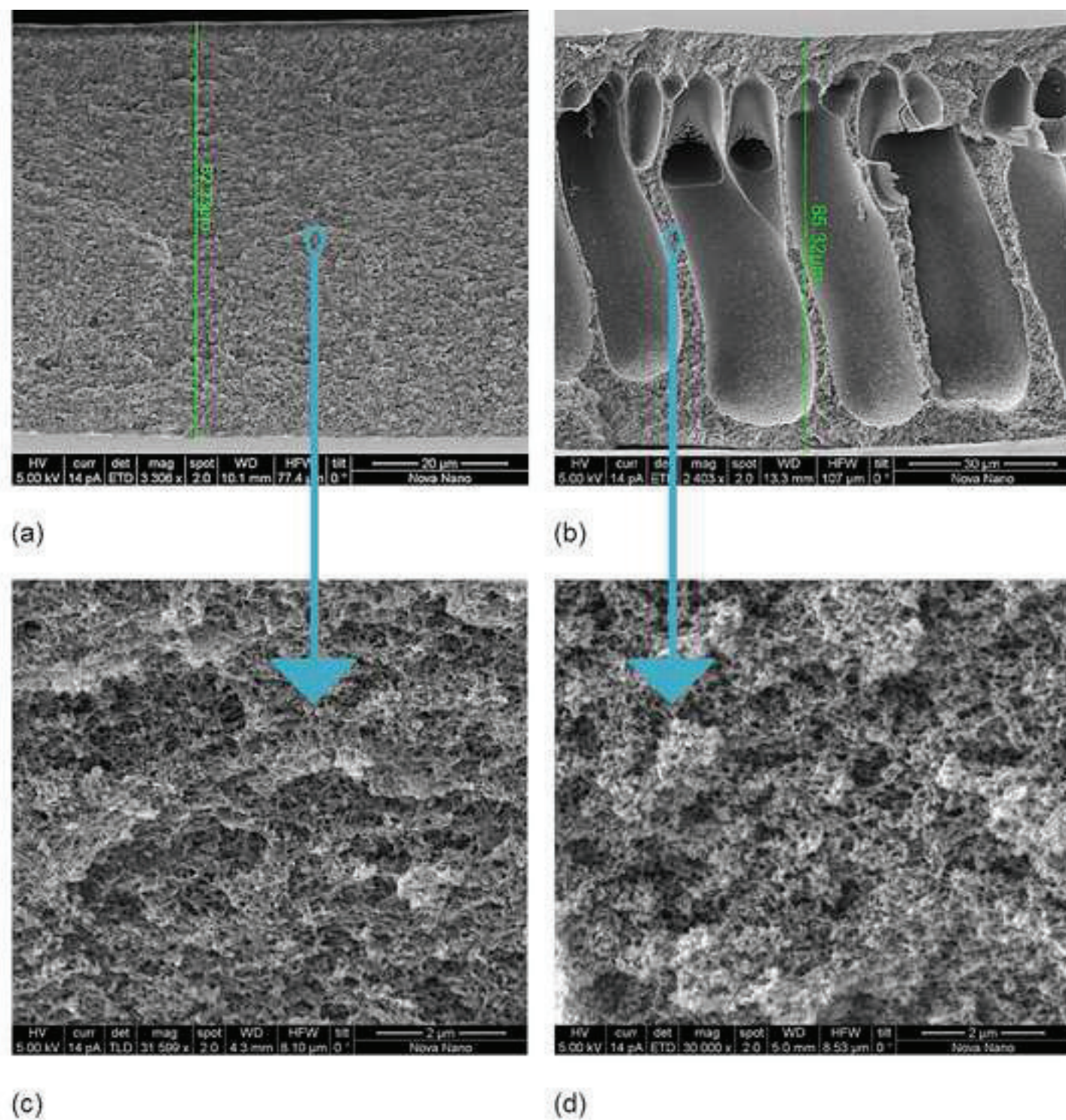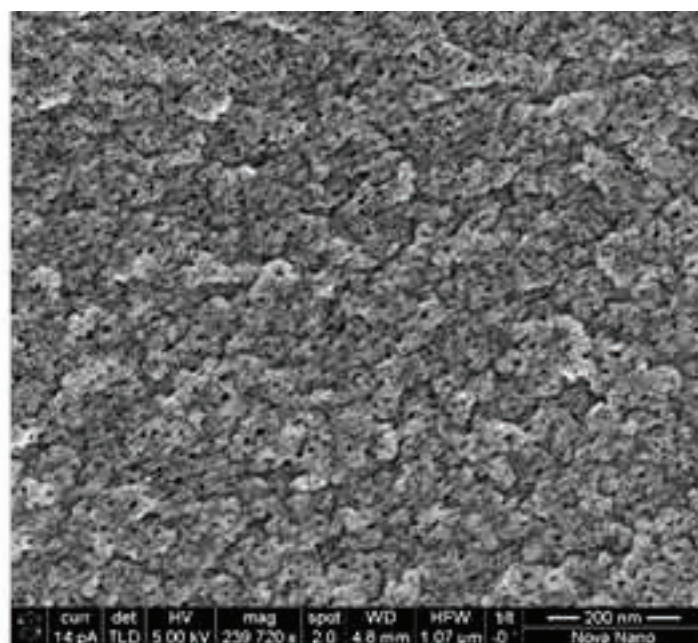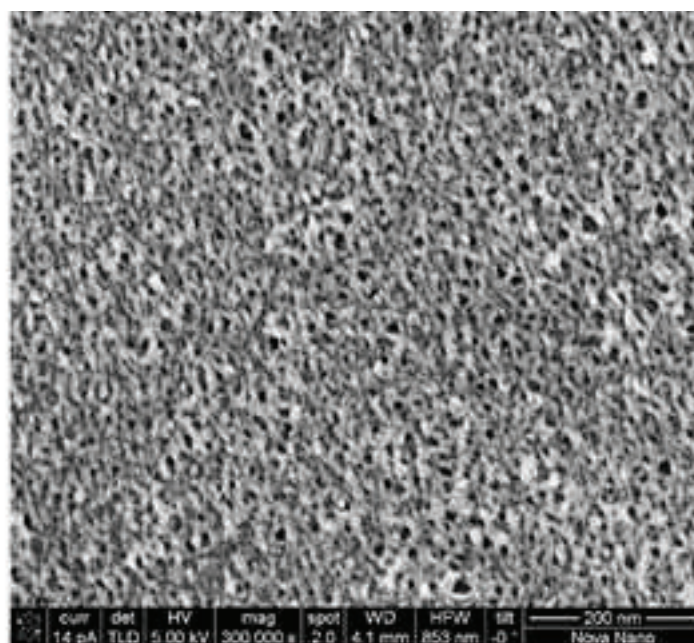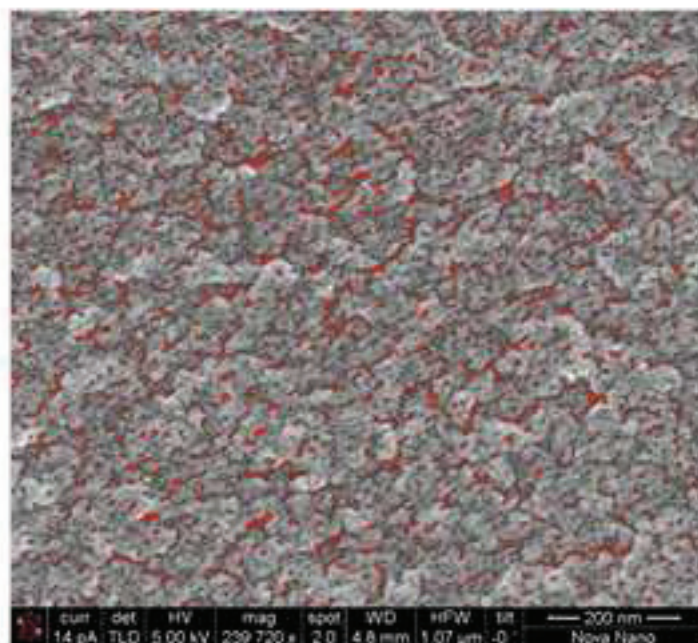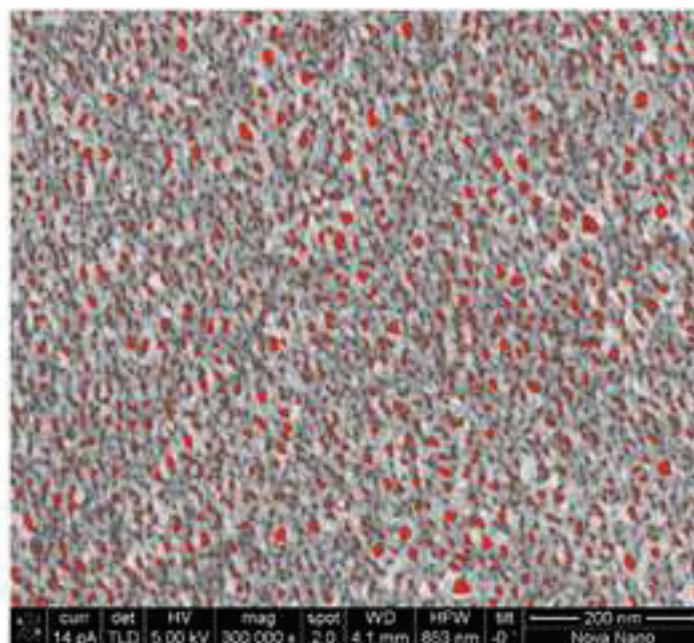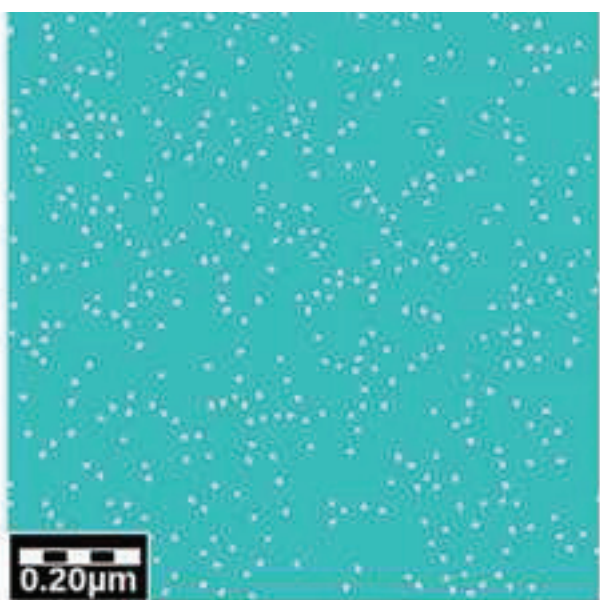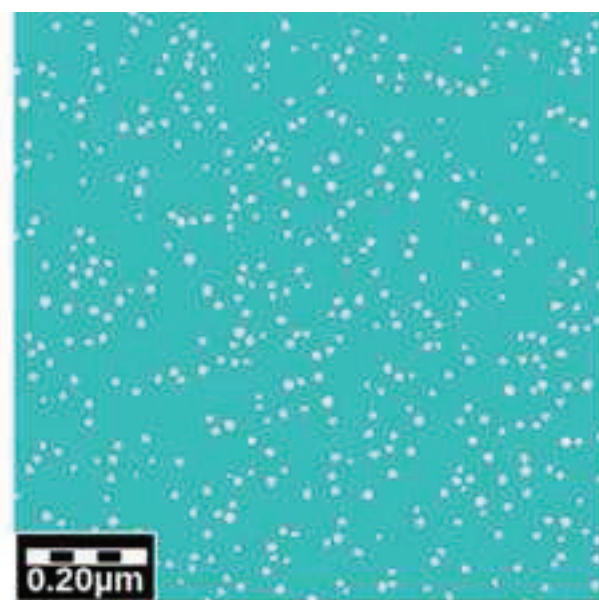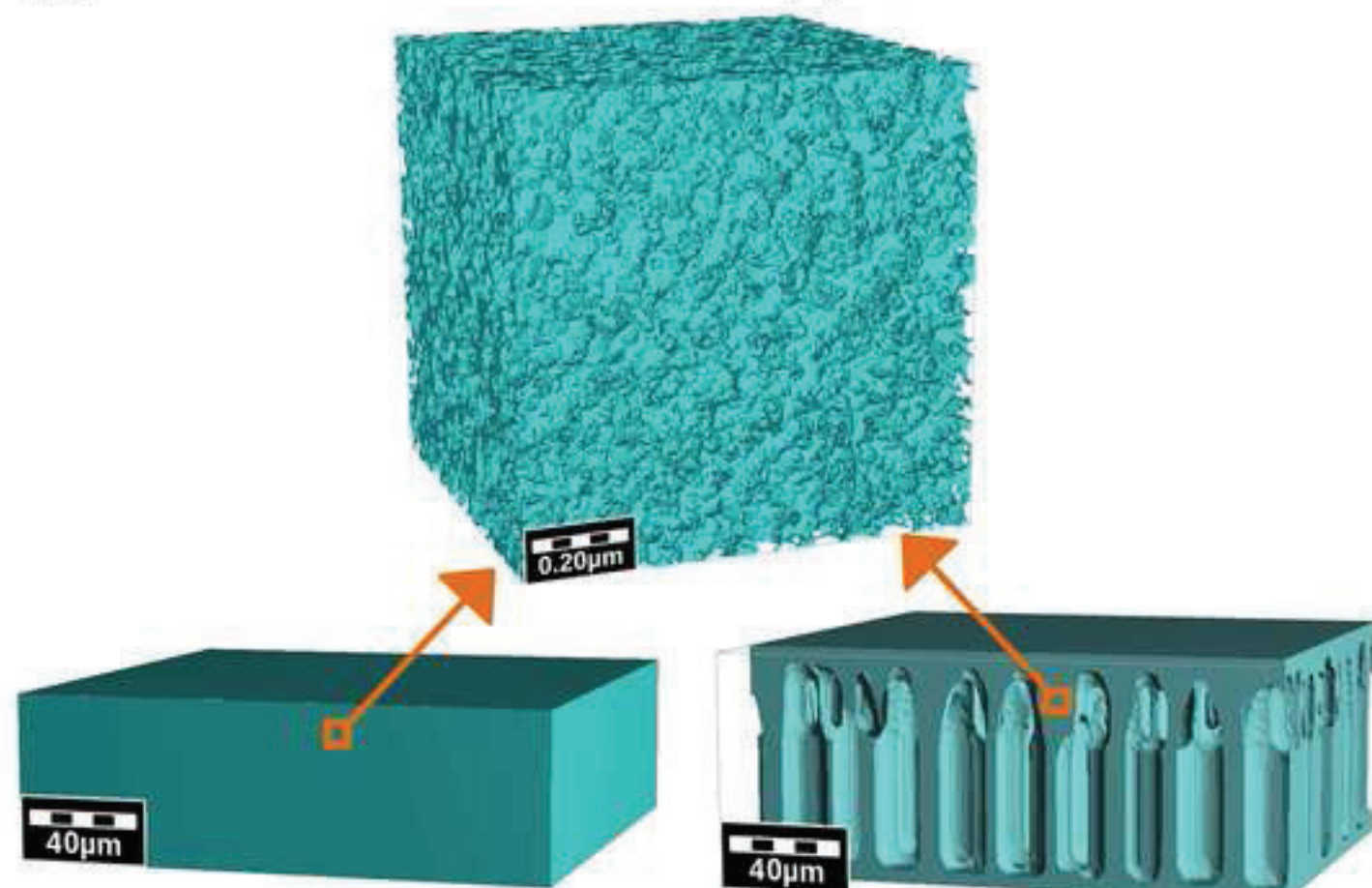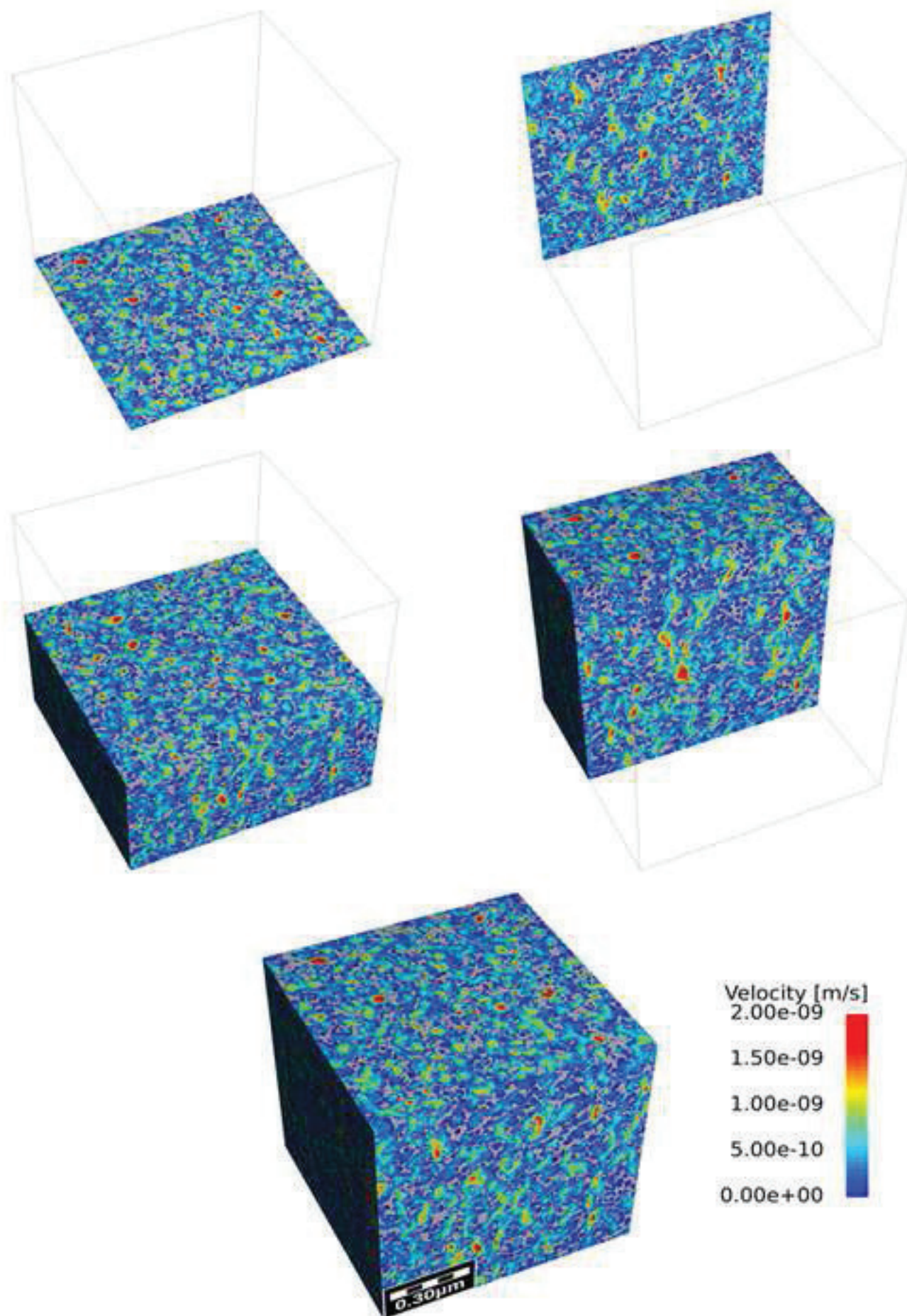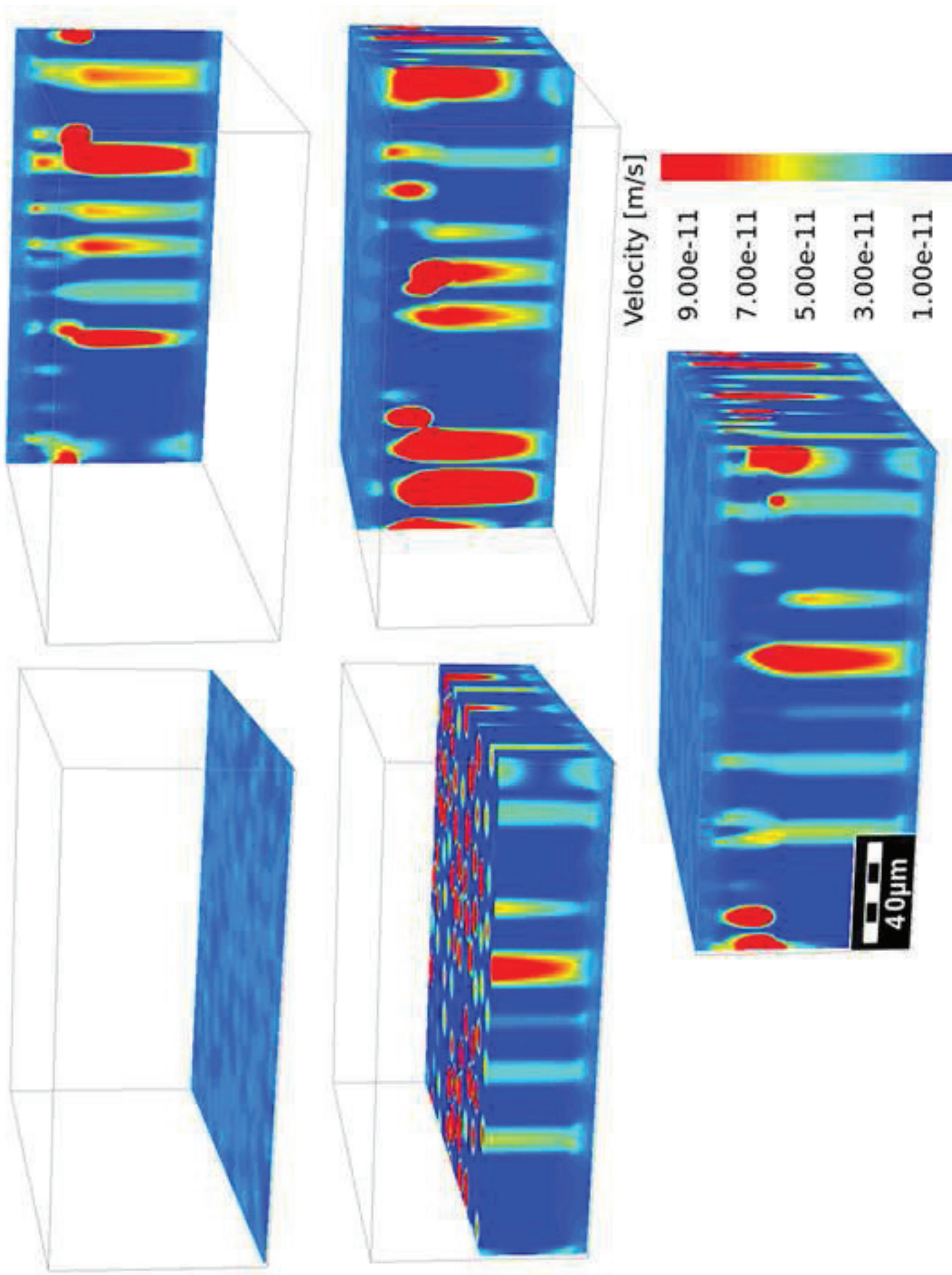
(a)

(b)

(c)

(d)

Figure2
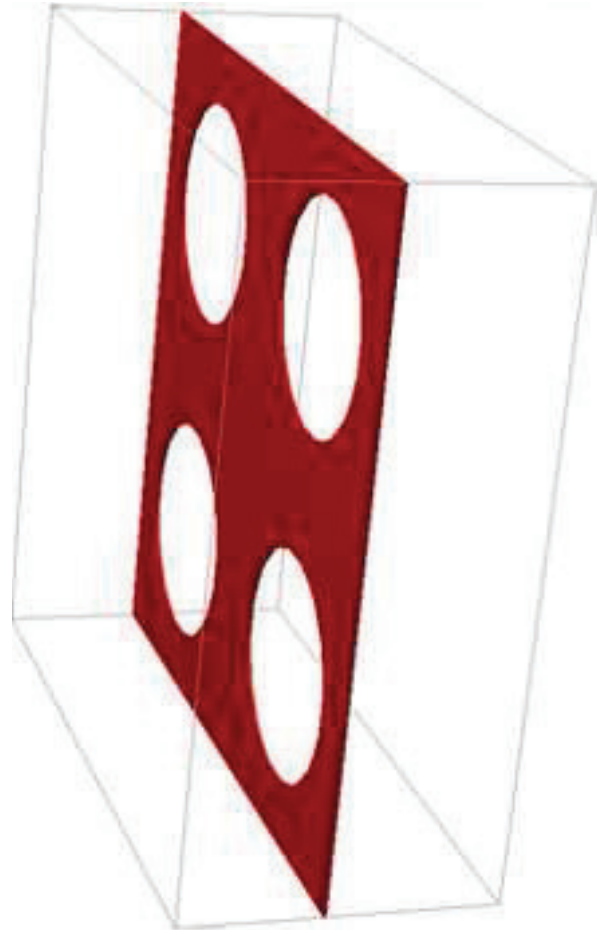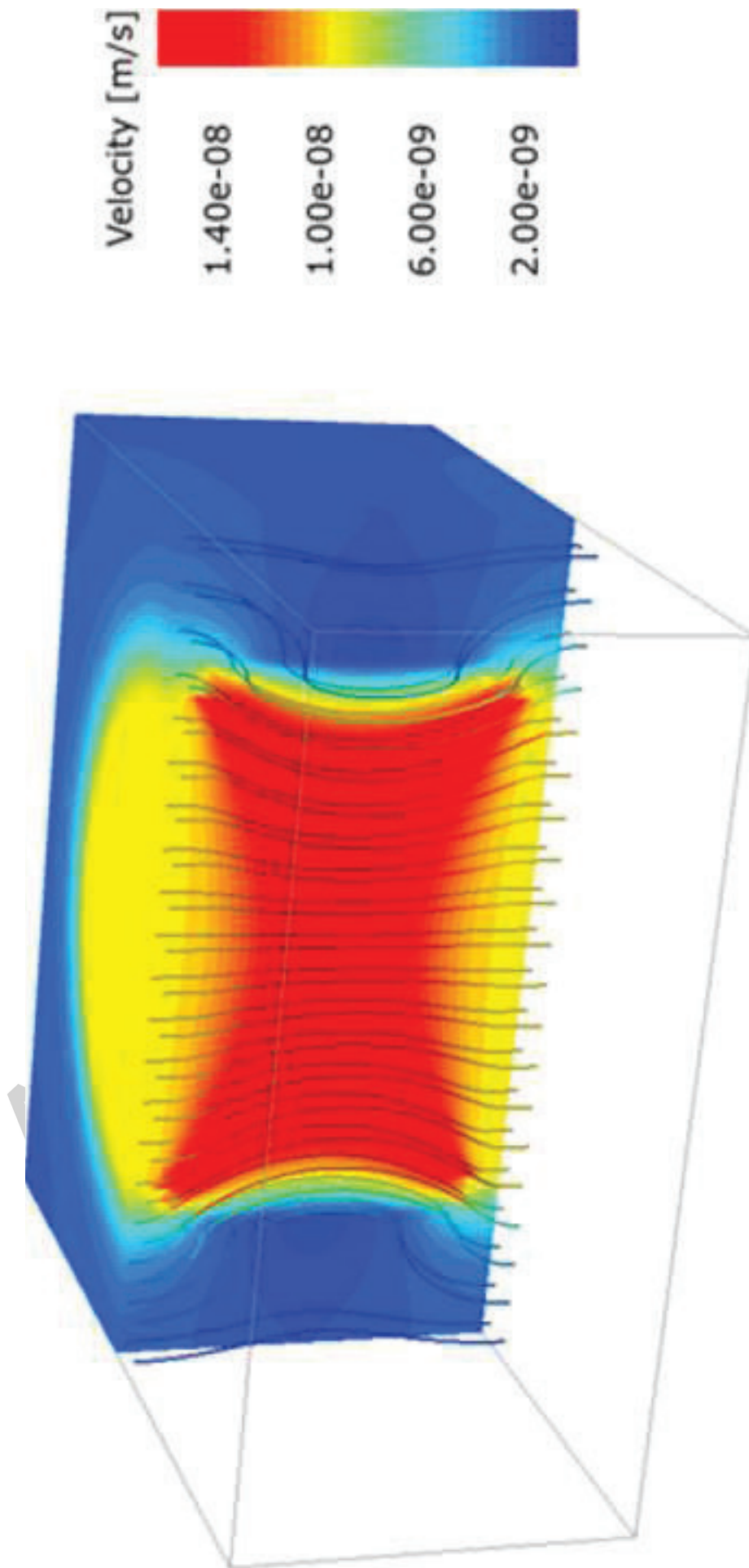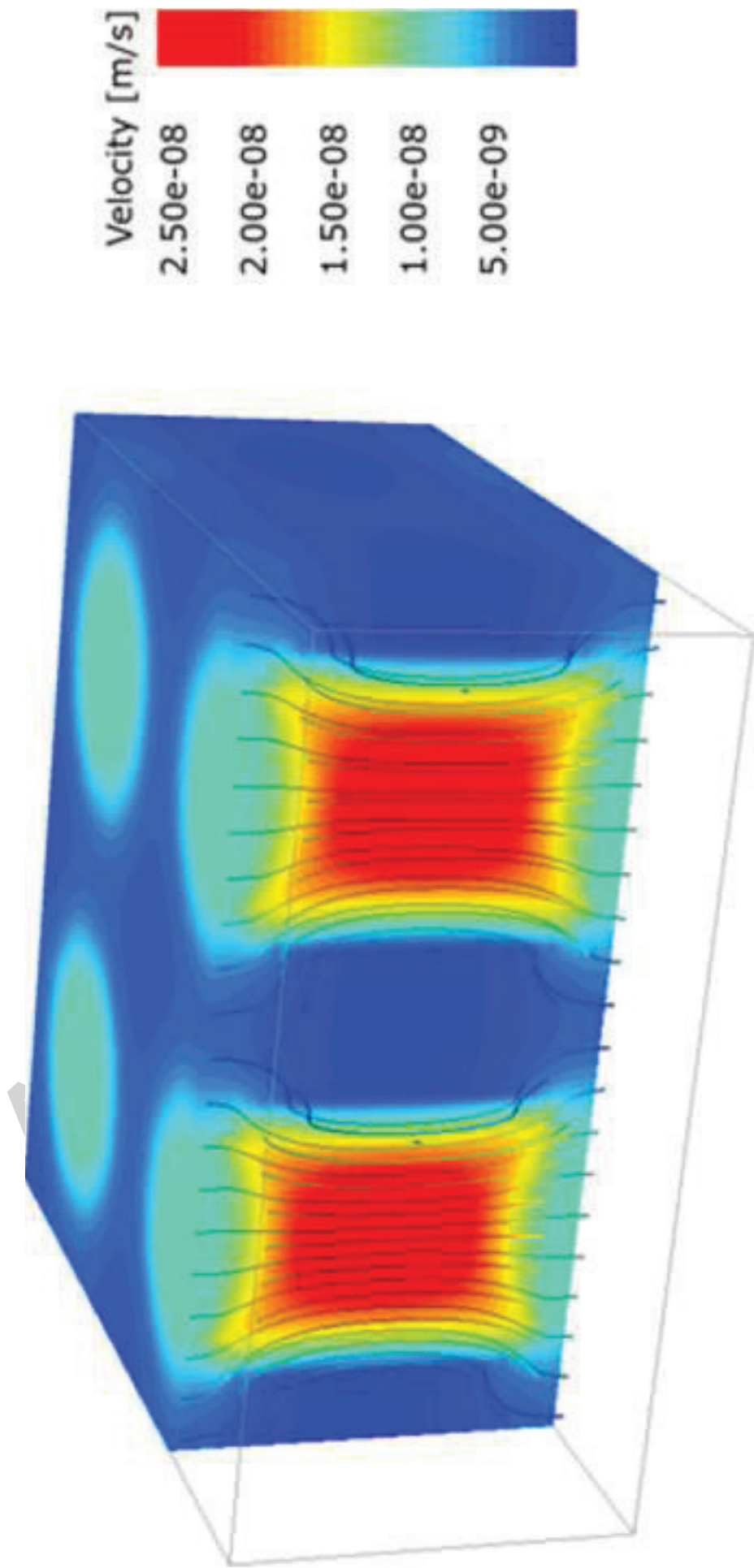Click here to download high resolution image

(a)

(b)

(c)

(d)

Figure3
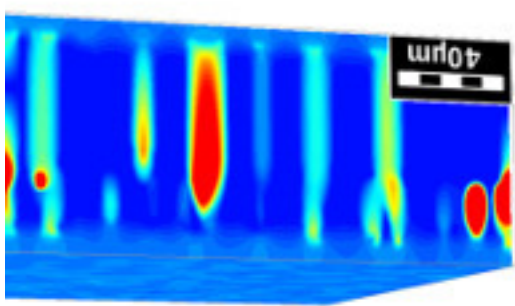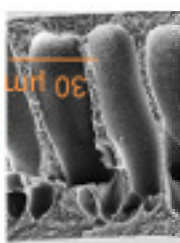Click here to download high resolution image

0.20μm

(a)

0.20μm

(b)

0.20μm

40μm

40μm

(c)

Figure4
Click here to download high resolution image

Velocity [m/s]
2.00e-09
1.50e-09
1.00e-09
5.00e-10
0.00e+00

0.30µm

Velocity [m/s]

9.00e-11
7.00e-11
5.00e-11
3.00e-11
1.00e-11

40μm

(a)

(b)

(c)

(d)

(a)

(b)

(c)

(d)

(a)   (b)   (c)

Velocity [m/s]

1.40e-08

1.00e-08

6.00e-09

2.00e-09
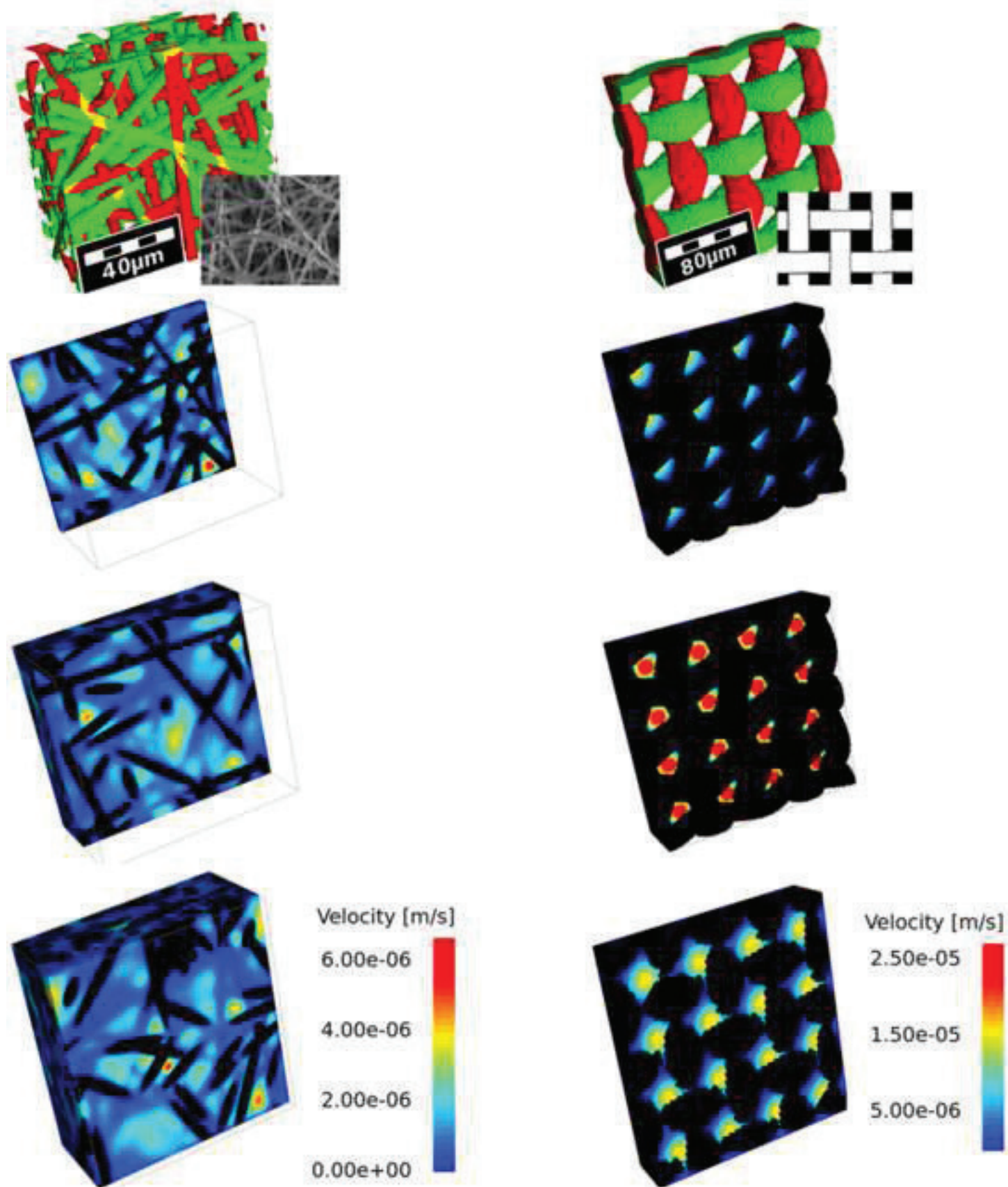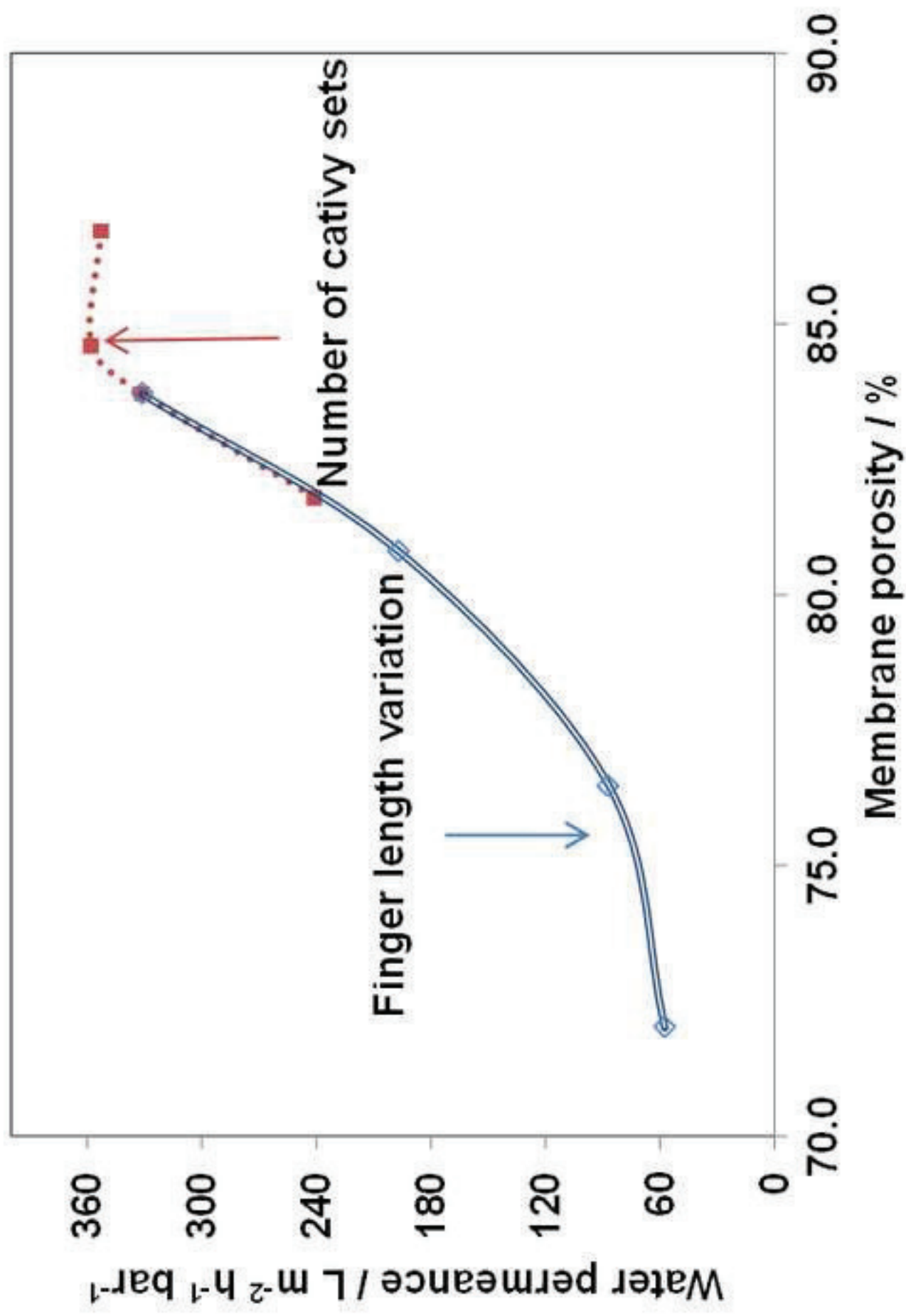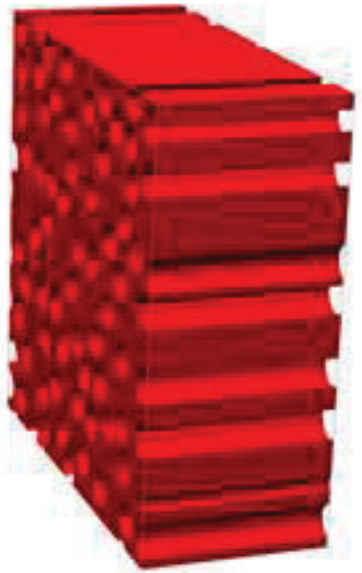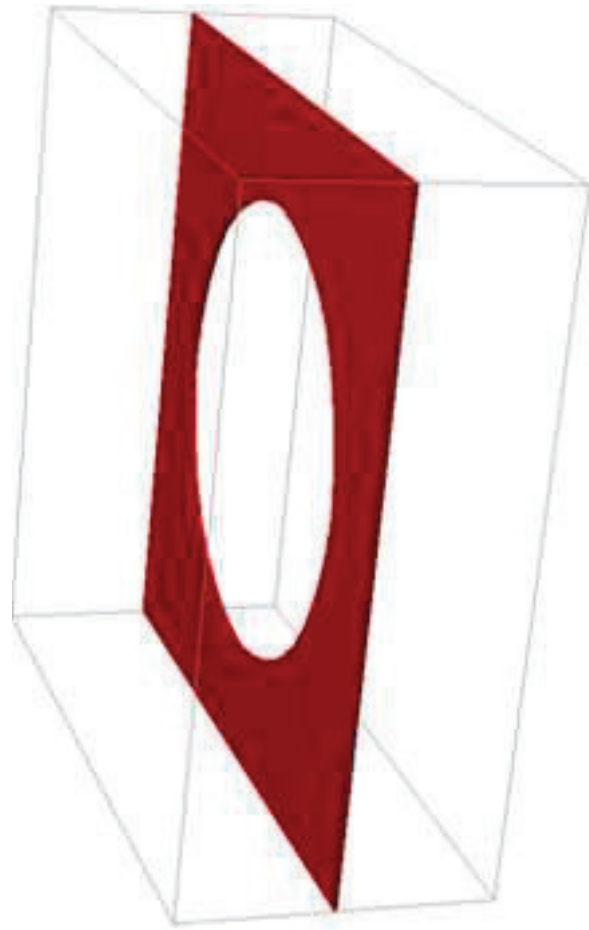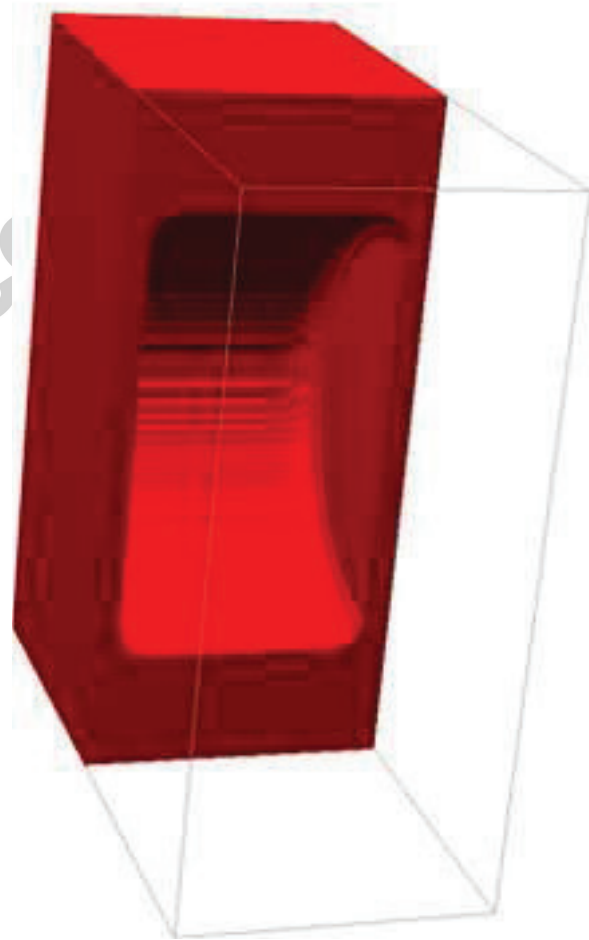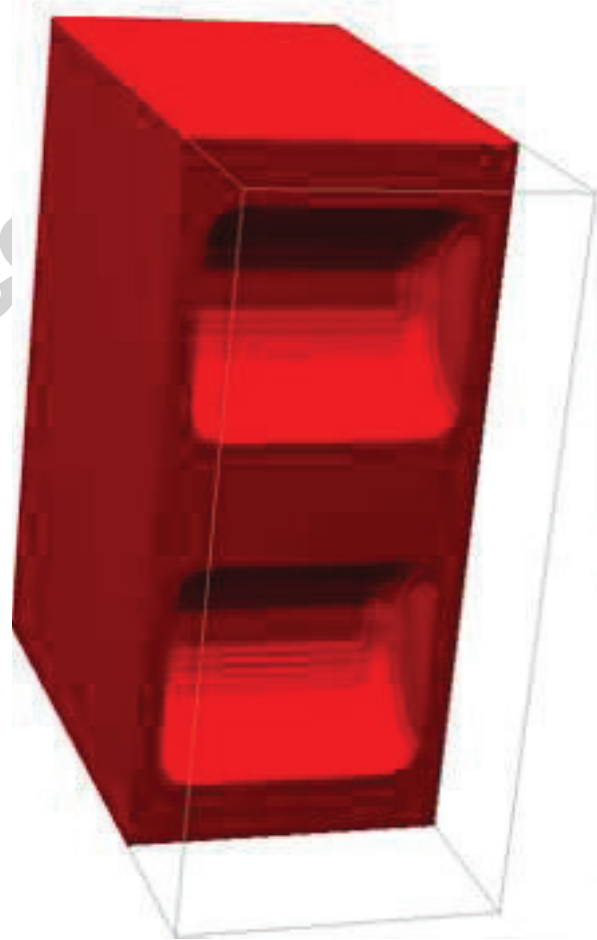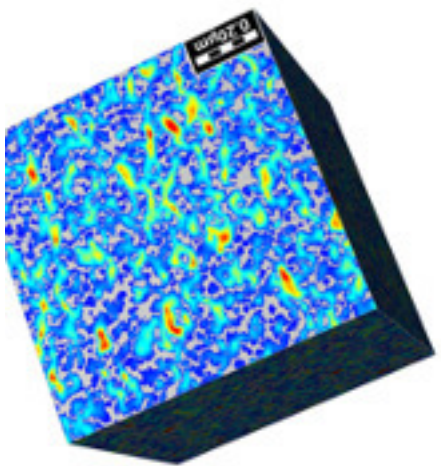
Flow Simulation at Pore S

3D Digital
Reconstruction

Membrane
ology